applied optics

Light manipulation with flat and conformal inhomogeneous dispersive impedance sheets: an efficient FDTD modeling

Samad Jafar-Zanjani, Jierong Cheng, and Hossein Mosallaei*

Department of Electrical and Computer Engineering, Northeastern University, 360 Huntington Avenue, Boston, Massachusetts 02115, USA
**Corresponding author: hosseinm@ece.neu.edu*

Received 29 January 2016; revised 24 February 2016; accepted 7 March 2016; posted 8 March 2016 (Doc. ID 258340); published 7 April 2016

An efficient auxiliary differential equation method for incorporating 2D inhomogeneous dispersive impedance sheets in the finite-difference time-domain solver is presented. This unique proposed method can successfully solve optical problems of current interest involving 2D sheets. It eliminates the need for ultrafine meshing in the thickness direction, resulting in a significant reduction of computation time and memory requirements. We apply the method to characterize a novel broad-beam leaky-wave antenna created by cascading three sinusoidally modulated reactance surfaces and also to study the effect of curvature on the radiation characteristic of a conformal impedance sheet holographic antenna. Considerable improvement in the simulation time based on our technique in comparison with the traditional volumetric model is reported. Both applications are of great interest in the field of antennas and 2D sheets.

OCIS codes: (000.4430) Numerical approximation and analysis; (260.3090) Infrared, far; (160.3918) Metamaterials; (310.6845) Thin film devices and applications; (240.6690) Surface waves.

http://dx.doi.org/10.1364/AO.55.002967

1. INTRODUCTION

Electromagnetic simulation of ultrathin (practically 2D) structures, using volume-discretization techniques, such as the finite-difference time-domain (FDTD) method [1], has always been of great challenge. The reason lies in the fact that, the volume mesh size in the direction perpendicular to these 2D sheets needs to be considered extremely small in order to model the nearly zero thicknesses of these structures. A representative schematic is depicted in Fig. 1.

Some possible solutions to address this challenge in the context of FDTD are using nonuniform grids, and subcell technique [2–5]. Yet the issue is that most of these structures are essentially 2D, and considering either a locally small or subcell thickness for them can be both computationally inefficient and inaccurate, especially for 2D resonant nanostructures where aspect ratio plays a key role. Meanwhile, taking advantage of the fact that the electromagnetic fields are updated for individual nodes (spatial sampling points) during the time marching loop of FDTD, it is possible to treat an impedance sheet as a 2D layer in the problem space (Fig. 1). This approach is the closest model to the actual structure, and, unlike the former methods, there will not be any approximation involved in the modeling procedure due to considering a thickness for the impedance sheet.

Many inspiring works have already been published on modeling thin material layers in FDTD. Most of them have been applied to study electrical and/or thermal properties of graphene layers and devices [6–9]. This paper presents a generalized formulation based on the ADE-FDTD technique, which is consistent with the conventional models of optical dispersion and also can be used to study a given condensed material system by fitting a few rational polynomial terms [1,10–12] to its arbitrary surface conductivity. This feature enables accurate modeling of various 2D materials with complicated dispersion response, such as graphene, molybdenum disulphide (MoS_2), and hexagonal boron nitride (h-BN) [13,14], or a heterogeneous combination of them and on substrate. It can also represent the equivalent surface impedance of optical metasurfaces without considering their actual inclusions (nanoscatterers or nanoantennas). This advantage also obviates the need for utilizing fine mesh to handle detailed structure of those inclusions. More specifically, the presented model in this paper for surface conductivity, with the capabilities previously mentioned, has not been proposed in previously published works. One of the motivations for exploiting this formulation arises from cases where a 2D sheet with a specific dispersion model has an interface with another sheet or bulk material, possessing a distinct dispersion characteristics.

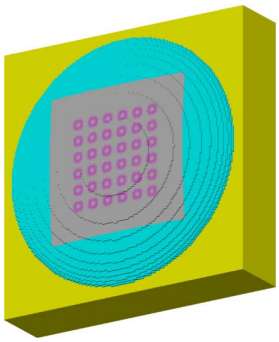

Fig. 1. Yee grid model of a representative conformal inhomogeneous impedance sheet (gray background sheet patterened with violet rings) supported by a dielectric structure.

Utilizing a general dispersion model facilitates the precise treatment of such interfaces.

Formulation of the proposed method is presented in Section 2. Section 3 provides numerical characterization of some novel optical devices using this method. Finally, a summary is given in Section 4.

2. FORMULATION

Consider an inhomogeneous dispersive impedance sheet located perpendicular to the z axis at $z = z_0$. By definition,

$$\vec{E}^{(t)}(\omega)|_{z=z_0} = \underline{\underline{Z_{\text{sh}}}}(x, y, \omega)[\hat{n} \times (\vec{H}_2(\omega) - \vec{H}_1(\omega))], \tag{1}$$

where $\vec{E}^{(t)}$ is the tangential component of electric field $\underline{\underline{Z_{\text{sh}}}}(x, y, \omega)$ is the inhomogeneous sheet impedance tensor, and $\hat{n}$ is normal to the surface. The above equation can be equivalently written as

$$\vec{J}_s(\omega) = \underline{\underline{\sigma_s}}(x, y, \omega)\vec{E}^{(t)}(\omega)|_{z=z_0}, \tag{2}$$

where $\vec{J}_s(\omega)$ is the surface current density on the impedance sheet and

$$\underline{\underline{\sigma_s}}(x, y, \omega) \triangleq \underline{\underline{Z_{\text{sh}}}}^{-1}(x, y, \omega). \tag{3}$$

Hereafter, we will omit the x and y dependence of the surface conductivity for the sake of conciseness; although a general inhomogeneous model is considered for the impedance sheet in this paper. Furthermore, suppose that the impedance sheet is located at an electric field plane of the Yee grid, as shown in Fig. 2. For a diagonally anisotropic impedance sheet, one can write the conductivity tensor as

$$\underline{\underline{\sigma_s}}(\omega) = \hat{x}\hat{x}\,\sigma_{xx}(\omega) + \hat{y}\hat{y}\,\sigma_{yy}(\omega). \tag{4}$$

Integral form of the Ampere's law can be used to obtain the update equations for electric fields. For example, for x component of the electric field in Fig. 2, we have

$$\oint_C \vec{\mathcal{H}} \cdot \mathrm{d}\vec{l} = \iint_S \epsilon \frac{\partial \vec{\mathcal{E}}}{\partial t} \cdot \mathrm{d}\vec{S} + \iint_S \vec{\mathcal{J}} \cdot \mathrm{d}\vec{S}, \tag{5}$$

where S is the shaded area in the Fig. 2, which is enclosed by path C, ϵ is the permittivity of the surrounding medium, and [7]

$$\vec{\mathcal{J}} \cdot \hat{x} = \sigma\mathcal{E}_x + \mathcal{J}_{sx}\delta(z - z_0). \tag{6}$$

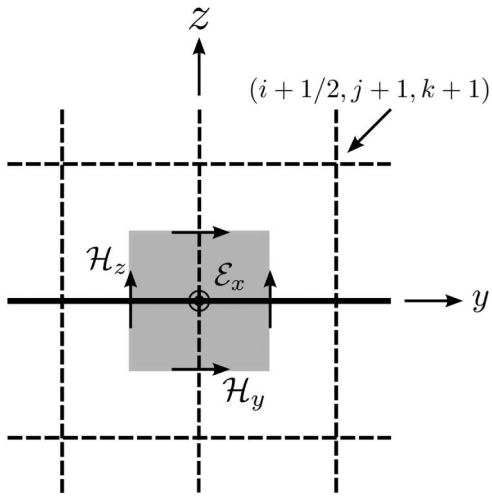

Fig. 2. 2D impedance sheet (solid line) residing at an electric field plane of the Yee grid.

Here, $\vec{\mathcal{J}}$ is volume current density, σ is the conductivity of the surrounding medium, and $\mathcal{J}_{sx}$ is the x component of the surface current density on the 2D sheet. Due to the continuity of the tangential component of electric field across the 2D sheet, $\mathcal{E}_x$ can be considered approximately constant over the integration area. In addition, magnetic field components along each edge of C can be approximated by the value at the center of that edge. Thus, after some manipulations,

$$(\nabla \times \vec{\mathcal{H}})_x\Big|_{i+1/2,j,k}^{n+1/2} = \epsilon\frac{\partial \mathcal{E}_x}{\partial t}\Big|_{i+1/2,j,k}^{n+1/2} + \sigma\mathcal{E}_x\Big|_{i+1/2,j,k}^{n+1/2} + \frac{1}{\Delta z}\mathcal{J}_{sx}\Big|_{i+1/2,j,k}^{n+1/2}, \tag{7}$$

where $(\nabla \times \vec{\mathcal{H}})_x$ is the x component of $\nabla \times \vec{\mathcal{H}}$; and Δy, Δz are FDTD cell sizes in y and z directions, respectively. Note that, in Eq. (7), the Ampere's law is evaluated at $n + 1/2$ time step.

On the other hand, according to Eqs. (2) and (4),

$$\frac{1}{\Delta z}J_{sx}(\omega) = \frac{\sigma_{xx}(\omega)}{\Delta z}E_x(\omega)\Big|_{z=z_0}. \tag{8}$$

In the most general case, $\sigma_{xx}(\omega)/\Delta z$ in Eq. (8) can be modeled as [4]

$$\frac{\sigma_{xx}(\omega)}{\Delta z} = \sigma_0 + \sum_{k=1}^{K}\frac{a_{2k}(j\omega)^2 + a_{1k}(j\omega) + a_{0k}}{b_{2k}(j\omega)^2 + b_{1k}(j\omega) + b_0 k}. \tag{9}$$

Here, σ_0 is a constant, and we have assumed that at least one of b_{2k} or b_{1k} to be unequal to zero. In other words, one can write from Eqs. (8) and (9),

$$\frac{1}{\Delta z}J_{sx}(\omega) = \sigma_0 E_x(\omega) + \sum_{k=1}^{K}J_{x,k}(\omega), \tag{10}$$

where

$$J_{x,k}(\omega) = \frac{a_{2k}(j\omega)^2 + a_{1k}(j\omega) + a_0 k}{b_{2k}(j\omega)^2 + b_{1k}(j\omega) + b_0 k}E_x(\omega). \tag{11}$$

The required ADE for $\mathcal{J}_{x,k}(t)$ is obtained by converting Eq. (11) to time domain [4]

$$\left[b_{2k}\frac{\partial^2}{\partial t^2}+b_{1k}\frac{\partial}{\partial t}+b_{0k}\right]\mathcal{J}_{x,k}(t) = \left[a_{2k}\frac{\partial^2}{\partial t^2}+a_{1k}\frac{\partial}{\partial t}+a_{0k}\right]\mathcal{E}_x(t). \tag{12}$$

Using the central difference procedure for time derivatives in Eq. (12), we have

$$\frac{b_{2k}}{\Delta t^2}(\mathcal{J}_{x,k}^{n+1}-2\mathcal{J}_{x,k}^{n}+\mathcal{J}_{x,k}^{n-1})+\frac{b_{1k}}{2\Delta t}(\mathcal{J}_{x,k}^{n+1}-\mathcal{J}_{x,k}^{n-1})+b_{0k}\mathcal{J}_{x,k}^{n} = \frac{a_{2k}}{\Delta t^2}(\mathcal{E}_x^{n+1}-2\mathcal{E}_x^{n}+\mathcal{E}_x^{n-1})+\frac{a_{1k}}{2\Delta t}(\mathcal{E}_x^{n+1}-\mathcal{E}_x^{n-1})+a_{0k}\mathcal{E}_x^{n}. \tag{13}$$

Solving Eq. (13) for $\mathcal{J}_{x,k}^{n+1}$, we obtain:

$$\mathcal{J}_{x,k}^{n+1} = \alpha_k\mathcal{J}_{x,k}^{n}+\xi_k\mathcal{J}_{x,k}^{n-1} + \frac{1}{2\Delta t}(\gamma_k\mathcal{E}_x^{n+1}-2\zeta_k\mathcal{E}_x^{n}+\tau_k\mathcal{E}_x^{n-1}), \tag{14}$$

where

$$\alpha_k = \frac{4b_{2k}-2b_{0k}(\Delta t)^2}{2b_{2k}+b_{1k}\Delta t}, \tag{15a}$$

$$\xi_k = \frac{b_{1k}\Delta t-2b_{2k}}{b_{1k}\Delta t+2b_{2k}}, \tag{15b}$$

$$\gamma_k = \frac{4a_{2k}\Delta t+2a_{1k}(\Delta t)^2}{2b_{2k}+b_{1k}\Delta t}, \tag{15c}$$

$$\tau_k = \frac{4a_{2k}\Delta t-2a_{1k}(\Delta t)^2}{2b_{2k}+b_{1k}\Delta t}, \tag{15d}$$

$$\zeta_k = \frac{4a_{2k}\Delta t-2a_{0k}(\Delta t)^3}{2b_{2k}+b_{1k}\Delta t}. \tag{15e}$$

From Eq. (7) and by using central difference method along with averaging, we determine

$$(\nabla\times\mathcal{H})_x^{n+1/2} = \epsilon\left(\frac{\mathcal{E}_x^{n+1}-\mathcal{E}_x^{n}}{\Delta t}\right)+(\sigma+\sigma_0)\left(\frac{\mathcal{E}_x^{n+1}+\mathcal{E}_x^{n}}{2}\right) + \sum_{k=1}^{K}\left(\frac{\mathcal{J}_k^{n+1}+\mathcal{J}_k^{n}}{2}\right). \tag{16}$$

Using Eqs. (10), (14), and (16), we can write the update equation for $\mathcal{E}_x$

$$\mathcal{E}_x^{n+1} = C_1\mathcal{E}_x^{n-1}+C_2\mathcal{E}_x^{n} + C_3\left\{(\nabla\times\mathcal{H})_x^{n+\frac{1}{2}}-\frac{1}{2}\sum_{k=1}^{K}\left[(1+\alpha_k)\mathcal{J}_{x,k}^{n}+\xi_k\mathcal{J}_{x,k}^{n-1}\right]\right\}, \tag{17}$$

where

$$C_1 = \frac{-\frac{1}{2}\sum_{k=1}^{K}\tau_k}{2\epsilon+\frac{1}{2}\sum_{k=1}^{K}\gamma_k+(\sigma+\sigma_0)\Delta t}, \tag{18a}$$

$$C_2 = \frac{2\epsilon+\sum_{k=1}^{K}\zeta_k-(\sigma+\sigma_0)\Delta t}{2\epsilon+\frac{1}{2}\sum_{k=1}^{K}\gamma_k+(\sigma+\sigma_0)\Delta t}, \tag{18b}$$

$$C_3 = \frac{2\Delta t}{2\epsilon+\frac{1}{2}\sum_{k=1}^{K}\gamma_k+(\sigma+\sigma_0)\Delta t}. \tag{18c}$$

Update equations similar to Eqs. (14) and (17) can be obtained for $\mathcal{J}_{y,k}$ and $\mathcal{E}_y$. Having these update coefficients, x and y components of the electric filed, exactly on the impedance sheet, are updated by the three-step ADE-FDTD algorithm [1]. Conventional FDTD is used to time-step field components other than those mentioned above.

3. NUMERICAL RESULTS AND DISCUSSION

A. Validation

The proposed formulation in the previous section was applied to several previously solved problems in the literature involving impedance sheets to assess the validity of the developed simulator: more specifically, studying a patterned graphene self-focus lens [15] for collimating the cylindrical surface wave generated by a point source to surface plane wave, and effects of electric field bias, substrate thickness, and permittivity on the reflection/transmission spectrum of a cross-shaped [3], ring, and double split ring resonator (DSRR) graphene frequency surface (GFSS) [4]. Padé approximation was also applied to wideband characterization of a graphene layer [10].

Here, we present two of those investigations in detail. In the first example, the transmission spectrum of a freestanding graphene sheet, illuminated by a normally incident plane wave, is compared with the analytical results for different values of electric bias field. We consider the intraband conductivity of graphene, which is the dominant term in the lower terahertz regime [16]. The amplitude and phase spectra calculated analytically, along with the numerical results obtained by the formulation of the previous section, are depicted in Fig. 3 for three different values of electric bias field. Complete agreement between analytical and FDTD results can be observed in the figure.

Moreover, the phase distribution of near-fields for the aforementioned graphene self-focus lens [15], obtained using the conventional 3D slab and 2D sheet models, are compared in Fig. 4. Figure 4(a) shows a schematic of the structure. Frequency of operation is 7 THz. Here, the background impedance sheet (gray) has a normalized sheet impedance $Z'_{\mathrm{sh1}} = Z_{\mathrm{sh1}}/\eta_0 = 2.34 + i10.75$ (η_0 is the wave impedance of free space), while this value is equal to $Z'_{\mathrm{sh2}} = Z_{\mathrm{sh2}}/\eta_0 = 0.64 + i3.77$ for the square patches (purple). The excitation is a z-polarized magnetic dipole, demonstrated with a yellow dot in the figure, and is placed 30 nm above the structure. Phase profile of the z-component of the electric field, in a plane 60 nm above the structure, calculated with 3D (volumetric approximation for the sheet) and 2D models are shown in Figs. 4(a) and 4(b), respectively. The resemblance of phase distributions is obvious in the figure. In addition, the required computational resources are reported in Table 1. Here, the FDTD cell sizes are equal to 30 nm in both y and z directions. On the other hand, the cell size in the x direction is 9 nm for the 3D and 30 nm for

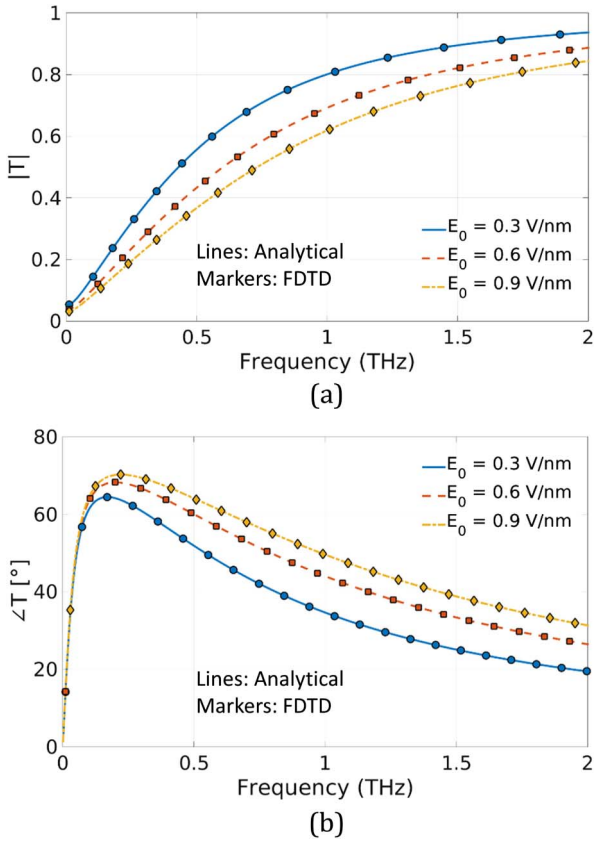

Fig. 3. (a) Amplitude and (b) phase spectra of a freestanding graphene sheet illuminated by normal incidence of a plane wave, for different values of electric bias field, as specified in the figure. Lines in both plots represent analytical solutions, while markers correspond to the numerical FDTD results.

the 2D model. The FDTD time-step is 0.023 fs for the 3D model, and 0.049 fs for the 2D model. Computations were performed by GPU version of our developed code on a workstation equipped with Nvidia Tesla K40c GPU accelerator, 24 CPU cores operating at 2.3 GHz clock frequency and about 250 GB of memory. It is observed that using the 2D model in comparison with the 3D volumetric approximation can provide speed and memory improvements by a factor of about 4; where the 2D technique is also more accurate and additionally free of efforts, one may need to make with volumetric case to properly approximate the sheet. More complex structures will take even more advantage of our proposed method in terms of speed and memory improvements, as will be illustrated in later examples.

Next, the method is utilized to design and characterize two novel devices in the emerging field of optical antennas. Namely, a leaky-wave line source to radiate an isoflux sector beam by cascading three sinusoidally modulated reactance surfaces (SMRS) and also a conformal impedance sheet holographic antenna, which converts the fields of a point source to a directed beam in space by designing a curvature-related impedance sheet. To the best of our knowledge, none of these systems have been previously proposed in the literature. The above-mentioned devices are designed to operate at the far-infrared regime, due to experimental considerations and material dispersions. However, the underlying concepts are applicable to higher frequencies (e.g., visible range) with proper 2D sheets, as well. All of the simulations were performed by an in-house-developed FDTD package accelerated by GPU computing.

B. Broad-Beam Leaky-Wave Antenna

Sinusoidally modulated reactance surfaces (SMRS) [17] have long been utilized as leaky-wave antennas to generate highly directive radiation beams. The surface reactance of a 1D SMRS can be expressed as [18]

$$X_s = X_s^{\text{avg}}\left[1 + M\cos\left(\frac{2\pi x}{p} + \varphi\right)\right], \tag{19}$$

where X_s^{avg} is the average surface reactance, M is the modulation index, p is the periodicity of the surface, and φ is an arbitrary phase offset specifying the surface reactance at $x = 0$. Recently, a reconfigurable sinusoidally modulated graphene leaky-wave antenna was proposed [18], which takes advantage of DC biasing gates beneath a uniform monolayer of graphene to scan the directive beam of the antenna in the elevation plane.

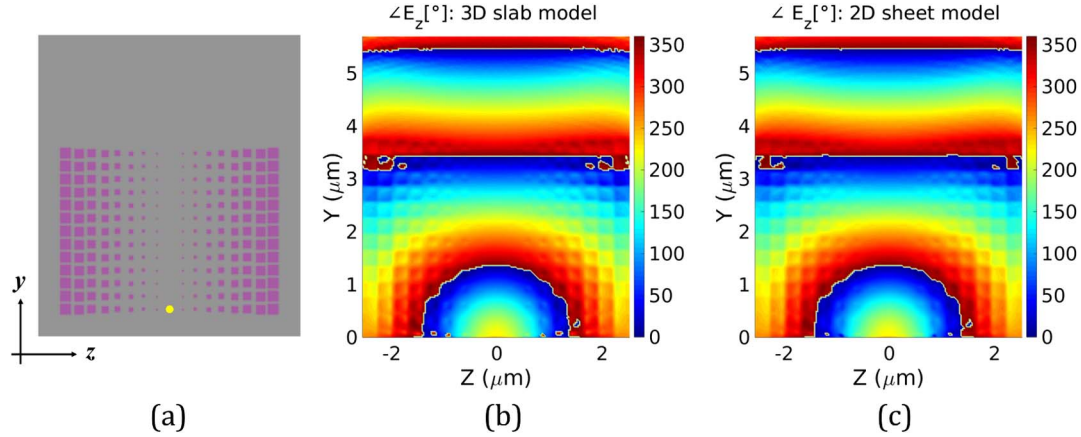

Fig. 4. (a) Schematic and phase distributions of z component of the electric field on a plane 60 nm above the impedance sheet self-focus lens, (b) obtained form 3D slab, and (c) 2D sheet models. Excitation is a z-polarized magnetic dipole located 30 nm above the structure at the position illustrated by a yellow dot in the schematic.

Table 1. Comparison Between Required Computational Resources for 3D Slab and 2D Sheet Models[a]

Scheme	Cell Size (nm)	Computation Time (min)	Memory (MB)
2D	30	53	923
3D	9	236	4171

[a]The reported cell sizes are in the direction perpendicular to the structure (x direction).

The idea was taken further in [19] to 2D beam scanning (scanning the beam in elevation and azimuth planes), by means of a practical 1D biasing scheme.

Leaky-wave antennas have also been extensively used [20–23] to synthesize broad-beam antennas, which radiate power evenly over a prescribed angular interval. More specifically, there are closed-form formulae in [20] derived by the geometrical-optics (GO) approximation for tapering the phase constant β, and attenuation constant α, along the antenna aperture, in order to generate an isoflux sector beam. Furthermore, a more rigorous technique based on the Orchard–Elliott synthesis method is proposed in [23] to tailor the electrical properties of a homogenized impedance sheet transferred on top of a grounded, uniaxial substrate tapered along the antenna length, which gives rise to arbitrary, prescribed radiation patterns. Here, we propose an infrared (IR) broad-beam antenna which is tunable by gate biasing, and obviates the need for a tapered uniaxial substrate.

A schematic of the designed leaky-wave antenna to radiate a broad beam at $f = 2$ THz is depicted in Fig. 5, which is comprised of an inhomogeneous lossless reactance sheet, deposited on a grounded substrate with a relative dielectric constant of $\epsilon_r = 3.8$ and a thickness of $h = 60$ μm. The overall aperture of the antenna is subdivided into three subapertures, each of them containing five periods of a SMRS with a constant period

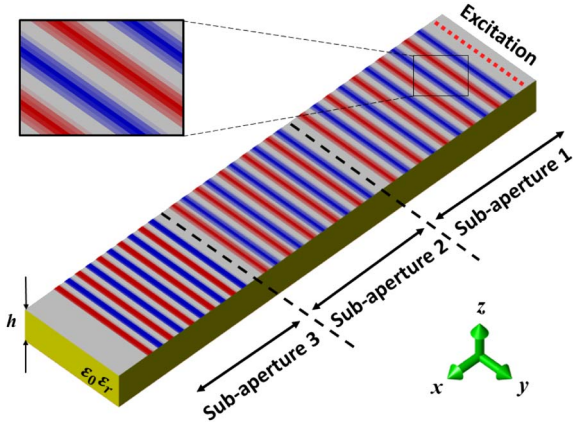

Fig. 5. Schematic of a broad-beam leaky-wave antenna constituted of an inhomogeneous lossless 2D sheet deposited on a grounded substrate. The overall aperture is subdivided into three subapertures, each containing five periods of a sinusoidally modulated reactance surface. Subapertures have the same average reactance and distinct values of periodicity and modulation index. Parameters: $f = 2$ THz, $h = 60$ μm, $\epsilon_r = 3.8$, $X_s^{\text{avg}} = 3.45\eta_0$, $p_1 = 50.3$ μm; $M_1 = 0.01$, $p_2 = 45.2$ μm; $M_2 = 0.37$, and $p_3 = 40.2$ μm; $M_3 = 0.5$.

and modulation index. The initial values of these constants are first determined based on the approximate formulae in [20] and then optimized to improve the performance of the antenna. Each of the constituent subapertures is designed by the same procedure that has been outlined in [18]. The average reactance is kept the same for all three subapertures and equal to that of the background sheet. It is well known that, by changing the period of a SMRS, the phase constant of the leaky mode and, equivalently, the radiation direction can be controlled. On the other hand, for a lossless sheet, leakage rate can also be altered as a function of the modulation index [17]. The main idea behind this design is to gradually alter the periodicity of consecutive SMRSs along the length of the line source to taper the phase constant, and at the same time, vary the modulation index to taper the leakage rate and, consequently, distribute the power evenly throughout the resultant broad beam. It is shown in [20] that, as we reduce the phase constant along the aperture, there will be a real focus point above the aperture where the rays from the three subapertures intersect, resulting in a sector beam, which is confined to the rays from the beginning and end of the line source. On the other hand, because the surface wave decays as a result of radiation, leakage rate should be increased along the aperture in order for the radiated power to be uniformly distributed over the radiated broad beam. The values of the periodicities are $p_1 = 50.3$ μm, $p_2 = 45.2$ μm, and $p_3 = 40.2$ μm for the first, second, and third subaperture, respectively, targeted for different radiation directions within the designed isoflux window. While the modulation indexes are $M_1 = 0.01$, $M_2 = 0.37$, and $M_3 = 0.5$, increasing from the first to the third subaperture to allow for the surface wave to propagate along the overall aperture without being radiated prematurely. The average surface reactance is chosen to be $X_s^{\text{avg}} = 3.45\eta_0$. Once the above-mentioned properties are decided, the sinusoidal distribution of surface reactance, X_s, can be mapped into the corresponding sheet reactance ($X_{\text{sh}} = 1/\sigma_s$) profile, using the curve plotted in Fig. 6, which is obtained by solving the dispersion relation given in Eq. (10) of [18]. Both axes are normalized to wave impedance of free space, $\eta_0 \approx 377\Omega$. It is worth noting that the mentioned curve is obtained for an infinite impedance sheet on top of

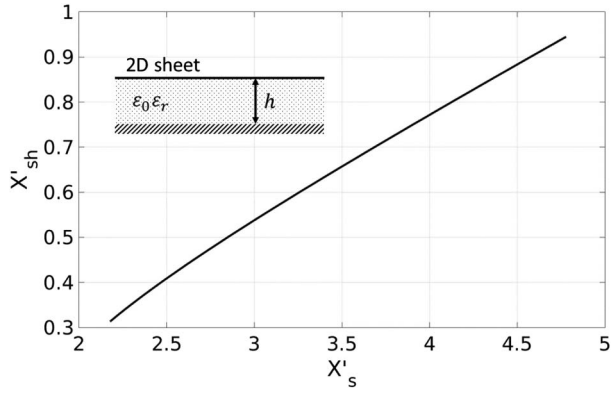

Fig. 6. Normalized sheet reactance ($1/\sigma_s$) as a function of normalized surface reactance. Both axes are normalized to the wave impedance of free space, $\eta_0 \approx 377\Omega$. The impedance sheet is considered to be lossless. Parameters: $f = 2$ THz, $\epsilon_r = 3.8$, $h = 60$ μm.

a grounded substrate [18]. In contrast, we have used finite strips of impedance sheet (as can be seen in the inset of Fig. 5). Hence, the mapping scheme involves an inevitable local periodicity approximation.

The FDTD problem space utilized to calculated the radiation pattern, has a size of 308, 12, and 40 cells in the x, y, and z directions, respectively. Cell size is considered uniform and equal to 2.52 μm. The computation time in this case is 210 s (3.5 min). On the other hand, suppose that the volumetric model is to be used for solving this problem. In this case, if we consider a thickness equal to 30 nm for the 2D sheet and, consequently, the cell size in the z direction, the scaled number of cells in the z direction is 3360, while the number of cells in other directions remains the same. The computation time in this case is approximated to be about 476,928 s (≈5.5 days), using the same computational resources. Hence, a speed-up factor of about 3 orders of magnitude is obtained. And, in addition, we need to mention that, in the traditional volumetric-based approach, one is still not sure how valid the assumed 30 nm thickness will be (until few trials can be performed and a saturation in result be observed). Thus, our proposed method is not only extremely fast but also very accurate (can realize the actual 2D sheet).

Radiation patterns of the antenna in the elevation ($\varphi = 0°$) plane, along with those of the subapertures, are plotted in Fig. 7. Because the structure is penetrated in to the perfectly matched layers (PMLs) in the x and y directions, the radiation pattern can be approximated by integrating on a flat plane above the aperture. Such evaluation of the radiation pattern has proven accurate by comparison with the result from a closed box. The modulation indexes are optimized in a way that a flat-top beam from 0° to 30° can be achieved. Although the subapertures have directions of maximum radiation at about, 8°, 17.7°, and 32.5°, the overall line source radiates a broad beam from −5° to 40°, approximately. The inset shows the area around the top of the beam. It is apparent that the previously mentioned design goal is achieved. It can also be deduced from the figure that the radiation beams from the second and third subapertures are merged in the overall pattern, while the role of the first one is not that pronounced, due to its small value of modulation index. It should be mentioned, however, that the presence of the first subaperture improves the performance of the antenna by providing an additional sample point for phase and attenuation constants, resulting in a more uniform distribution of radiated power over the considered angular interval.

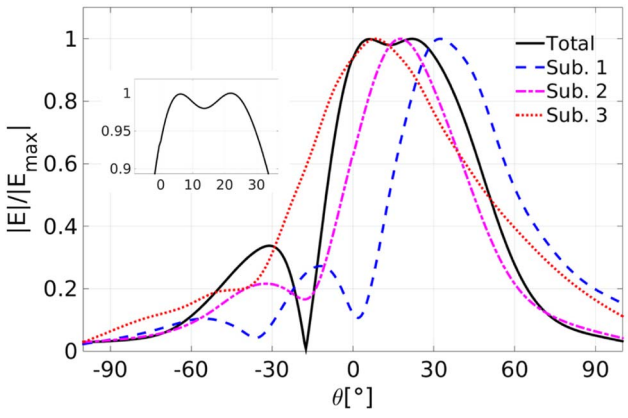

Fig. 7. Radiation pattern of the designed broad-beam leaky-wave antenna (Fig. 5) in the elevation ($\varphi = 0°$) plane, along with those of the subapertures. Flattop of the broad beam is enlarged in the inset.

Furthermore, the near-field plots of the antenna in the xz (perpendicular) and xy (parallel) planes are depicted in Figs. 8(a) and 8(b), in the middle of the y dimension and at the position of the aperture, respectively. The main broad beam, the sidelobe in the backward direction, and the segments of the aperture, where they have been originated from, can be observed in Fig. 8(a). It is also obvious from the figure that the first subaperture does not play a major role in the radiation of the antenna because of the small value of its modulation index. Although the impedance sheet is lossless, it can be seen in a Fig. 8(b) that the surface wave is decaying (being lost to radiation) toward the end of the aperture. Meanwhile, due to the proper choice of the modulation indexes, distribution of the surface wave along the whole aperture can be observed.

C. Conformal Hologram

The concept of holography has been widely employed in the microwave regime to design low-profile artificial impedance surfaces that are capable of radiating a prescribed output wave, when excited by a specific input wave [24]. The surface

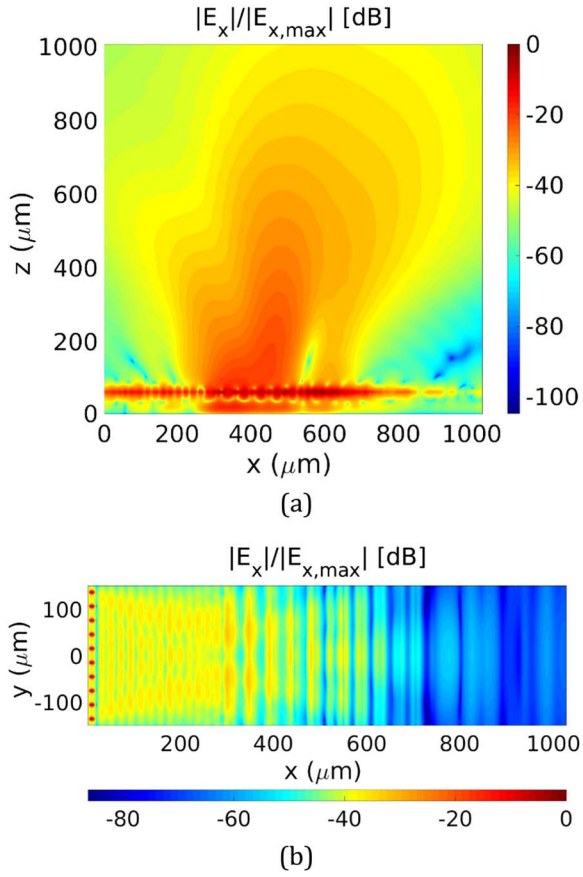

Fig. 8. Near-field plots of the broad-beam leaky-wave antenna of Fig. 5, plotted in (a) xz (perpendicular) and (b) xy (parallel) planes, in the middle of the y dimension, and at the position of the aperture, respectively.

impedance is tailored along the aperture by altering the properties of printed metallic inclusions (e.g., size or shape of metallic patches) on grounded substrates. Examples of conformal artificial impedance surface antennas can also be found in the literature [25,26]. These conformal antennas find application in areas where the antenna is needed to be mounted on curved surfaces, such as those of aircraft, cars, and the human body. The application of this technique in the terahertz frequencies has also been reported [27]. In this case, plasmonic subwavelength nanoantennas (nanoscatterers) are employed instead of their PEC counterparts in the microwave regime. Our goal here is to investigate the possibility of a conformal impedance sheet holographic antenna in the terahertz regime. The conventional characterization of conformal impedance sheets based on the volumetric model will be challenging, as the mesh size must be fine enough to resolve the sheet thickness and the curvature. On the other hand, utilizing the 2D sheet model, as we do in this work, will significantly simplify the task.

Distribution of the surface reactance along the conformal aperture of the antenna can be considered as the interference pattern of the input surface wave and the projection of the desired output wave on the surface. Mathematically [24],

$$X_s = X_s^{\text{avg}}[1 + M\Re\{\Psi_{\text{out}}\Psi_{\text{in}}^*\}], \tag{20}$$

where M is the modulation index (modulation depth) and Ψ_{in}, Ψ_{out} are the input surface wave and projection of the desired radiated wave on the conformal aperture, respectively. There will also be a surface resistance, R_s, due to the material loss of the impedance sheet [18], which is taken into account in FDTD simulations. Thus, the overall surface impedance can be considered as

$$Z_s = R_s + iX_s. \tag{21}$$

Surface reactance [Eq. (20)] of a point $\vec{r}$ on the conformal surface can also be expressed as [26]

$$X_s = X_s^{\text{avg}}[1 + M\cos(k_{\text{eq}}r - \vec{k}_0 \cdot \vec{r} + \phi)]. \tag{22}$$

Here, r is a scalar representing the distance along the surface from the source to the considered point, $\vec{r}$ is the position vector of the point, k_{eq} is the equivalent wavenumber seen by the surface wave, $\vec{k}_0$ is the wavevector in the desired direction of radiation, and ϕ is an arbitrary phase offset, which specifies the reactance value at the source position [24]. After calculating the distribution of surface reactance from Eq. (22), it can be mapped to the sheet reactance ($X_{\text{sh}} = 1/\sigma_s$), as will be shown in the following. Because we use finite patches of an impedance sheet to sample the surface impedance distribution along the aperture, the mapping scheme involves local periodicity approximation.

Figure 9 shows a schematic of the designed conformal hologram consisting of a lossy sinusoidally modulated impedance surface deposited on a grounded curvilinear substrate with $h = 60$ μm thickness, radius of curvature $R = 5\lambda_0$, and relative dielectric constant of $\epsilon_r = 2.25$; working at the central frequency of $f = 2$ THz. The hologram is 450 μm ($3\lambda_0$) wide in the x and y directions. The purpose of this design is to have a pencil beam directed at $\theta_0 = 30°$ and $\phi = 0°$. The SMRS is chosen to have an average surface reactance $X_s^{\text{avg}} = 2.5\eta_0$ and a modulation index of $M = 0.35$. It is worth mentioning that the color

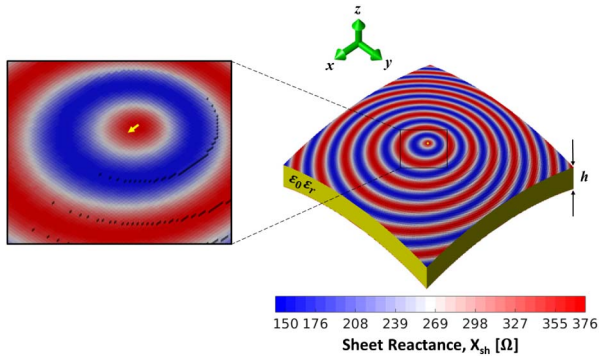

Fig. 9. Schematic of a conformal hologram, which is comprised of a lossy sinusoidally modulated impedance sheet, deposited on a curvilinear substrate. Excitation is an x-polarized dipole source very close to the highest point of the structure. Parameters: $f = 2$ THz, $h = 60$ μm, $\epsilon_r = 2.25$, $R = 5\lambda_0$, $X_s^{\text{avg}} = 2.5\eta_0$, and $M = 0.35$. Color bar shows the values of sheet reactance $X_{\text{sh}} = 1/\sigma_s$.

bar in Fig. 9 shows the values of sheet reactance, which is obtained after mapping the designed surface reactance by the curve depicted in Fig. 10. Therefore, it should not be mistaken for the surface reactance itself. The excitation is an x-polarized electric dipole located extremely close to the highest point of the structure (inset of Fig. 9).

The computation time for this model is 1762 s (≈30 min). Directivity patterns of the conformal hologram described above are plotted in Fig. 11. Figure 11(a) shows the Cartesian directivity pattern in the elevation ($\varphi = 0°$) plane. Two curves are noted in this figure. One of them, which is labeled "modified," represents a conformal hologram with the reactance distribution of Eq. (22). The other one is labeled "unmodified" and is the result of directly bending a flat holographic impedance sheet antenna, with the same dimensions in the x and y directions, to the same radius of curvature [27]. It can clearly be observed that the unmodified pattern shows a distribution of power in a large angular interval from approximately −40° to 40° and also a large unsought lobe at around 90°, which represents the edge effect. On the other hand, for the modified case, we observe a pencil beam directed at 30°, which is the

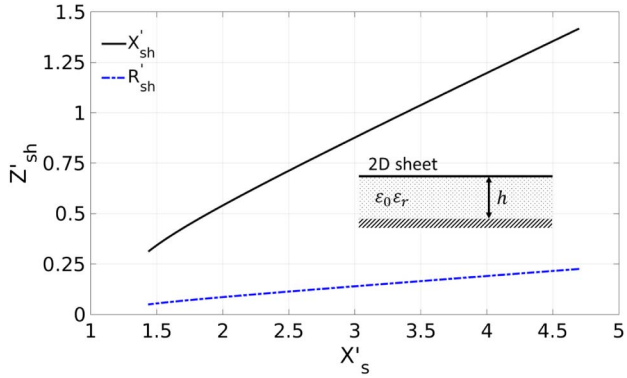

Fig. 10. Normalized sheet impedance ($1/\sigma_s$) as a function of the normalized surface reactance. Both axes are normalized to the wave impedance of free space, $\eta_0 \approx 377\Omega$. Parameters: $f = 2$ THz, $\epsilon_r = 2.25$, $h = 60$ μm.

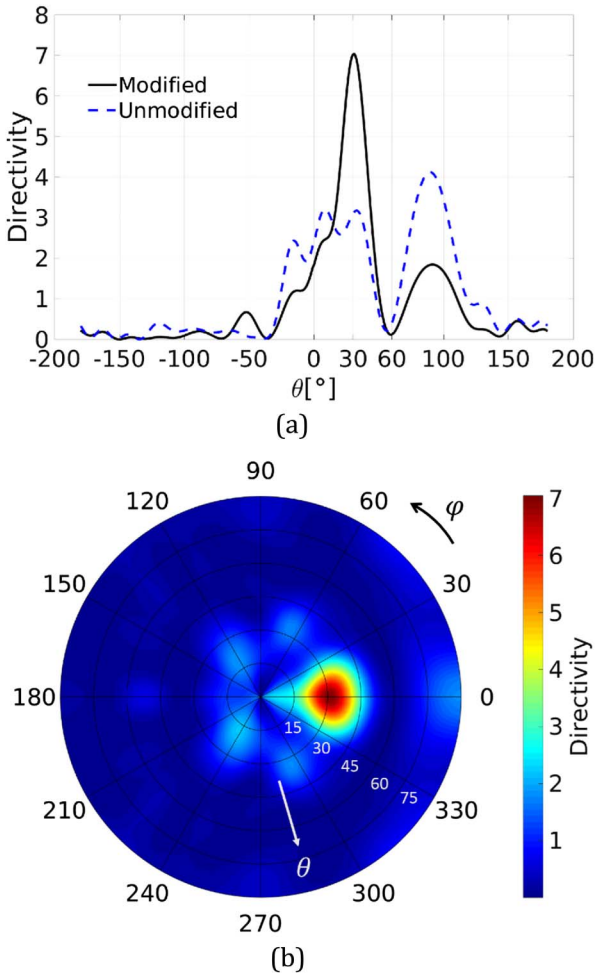

Fig. 11. (a) Cartesian directivity pattern of the hologram shown in Fig. 9 in the elevation plane ($\varphi = 0°$), for unmodified and modified surface impedance distributions. (b) 2D pseudo-color directivity pattern as a function of φ and θ corresponding to modified impedance distribution.

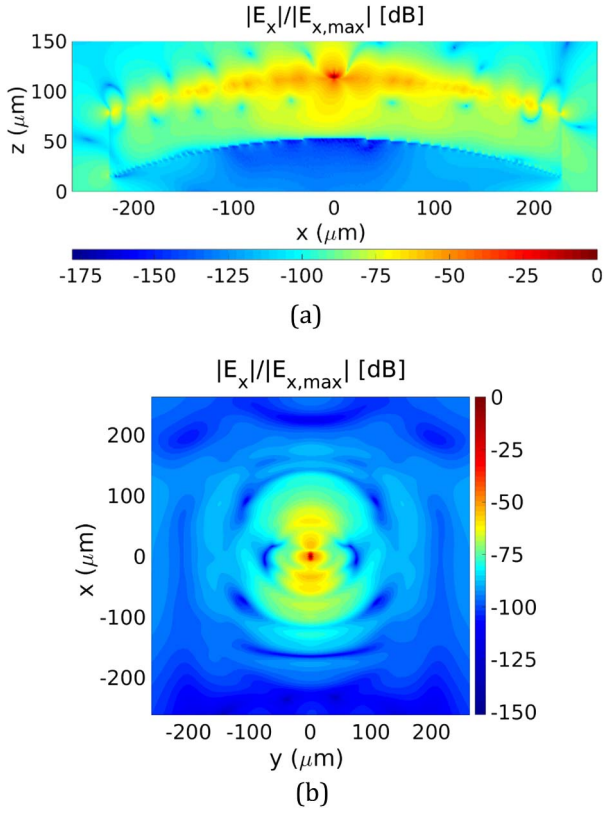

Fig. 12. Near-field plots of the conformal hologram of Fig. 9 in (a) perpendicular *xz* plane located in the middle of the *y* dimension and (b) *xy* plane very close to the highest point of the structure.

prescribed direction of desired radiation, and a very small edge effect compared with the unmodified case. The relatively low directivity of the antenna can be related to the material loss, which reduces the effective aperture size, and also small size of the physical aperture itself. A 2D pseudo-color directivity pattern as a function of θ and φ is also plotted in Fig. 11(b) for the case of modified impedance distribution. It is obvious that the radiated beam is well confined to $\varphi = 0°$, and also the sidelobe at 90° is negligible compared with the main pencil beam. This sidelobe can be attributed to the approximations that are involved in the modeling, such as inaccuracy in surface impedance mapping due to the curvature of the structure, staircasing error, and edge effect. The error caused by curvature becomes larger, as we consider a smaller radius of curvature, and the staircasing error can be reduced by considering a finer mesh or using more sophisticated meshing schemes. Furthermore, optical devices are usually fabricated on substrates that are much larger than the dimensions considered in the simulations here. We have considered a finite substrate here to be able to put the whole structure in a radiation box for calculating the radiation pattern. Although it is possible to approximate the radiation pattern by integrating on a plane above a flat antenna, instead of a whole radiation box, this approximation will not be valid in this case because of the curvature.

Finally, the near-field plots of the hologram in the perpendicular *xz* plane, which is located in the middle of the *y* dimension, and the *xy* plane, which is close to the highest point of the structure, are plotted in Figs. 12(a) and 12(b), respectively. It is obvious from Fig. 12(a) that the surface wave is being propagated along the curved surface to the end (and decayed due to the existence of lossy sheet). The utilized curve for sheet resistance is depicted in Fig. 10 [18]. Some radiation from the right edge of the structure can be observed [equivalent to the sidelobe at about 90° in the modified curve of Fig. 11(a)], which can be avoided in the practical case of a large substrate supporting the optical antenna, as discussed above. In addition, it can be seen that the right half of the hologram is radiating coherently in the direction of desired radiation. Figure 12(b) demonstrates an unsymmetrical behavior concerning the distribution of the near-fields over the aperture of the antenna. In other words, the surface wavefront is being propagated along the *x* axis. It is worth mentioning that, although it may not be so obvious in Fig. 9, the structure is not symmetrical with respect to φ, and also the exciting point source is polarized in the *x* direction. It is observed that, if the source has perpendicular polarization (*z* polarization), the radiation direction will

not obey the considered radiation angles. The reason can be described as the poor excitation of the TM surface wave in the latter case.

4. CONCLUSION

A unique FDTD-ADE formulation for successful modeling of inhomogeneous, dispersive impedance sheets is presented. The proposed formulation can easily be integrated in existing FDTD solvers and is general enough to handle various 2D sheet problems with arbitrary geometrical configurations and dispersion characteristics (and of practical interests to optics community). The proposed model illustrates significant computational speed and memory improvements in comparison with the traditional volumetric-based approach. In addition, it is accurate, as one does not have to assume a thickness for the sheet (and then through some study find the optimum value).

Novel designs in the emerging area of optical metasurfaces and nanoantennas, including a leaky-wave line-source designed to radiate a broad beam by cascading SMRS subapertures, along with a conformal holographic impedance sheet antenna, which converts the radiated fields of a small electric dipole to an arbitrarily directed pencil beam in space, are reported for the first time to the best of our knowledge. In both cases, good agreements between the design goals and obtained results are observed, which validates the accuracy of the proposed method and shows its power for efficient analysis of light manipulation with impedance sheets.

Funding. Air Force Office of Scientific Research (AFOSR) (FA9550-14-1-0349); Army Research Office (ARO) (MURI Award W911NF-14-0247).

Acknowledgment. The authors would like to express their sincere appreciation to Mr. Zhonglinag Chen for his valuable assistance regarding the development of the parallel, GPU computing enabled version of the codes in this work. The authors also gratefully acknowledge use of Tesla K40c GPU Accelerators provided by Nvidia Hardware Grant Program.

REFERENCES

1. A. Taflove and S. C. Hagness, *Computational Electrodynamics* (Artech House, 2005).
2. G. D. Bouzianas, N. Kantartzis, and T. Tsiboukis, "Subcell dispersive finite-difference time-domain schemes for infinite graphene-based structures," IET Microwaves Antennas Propag. **6**, 377–386 (2012).
3. T. Zhang, X.-H. Wang, Y. Guo, J. Hu, and W.-Y. Yin, "Improved FDTD method for studying on graphene frequency selective surface (GFSS) characteristics for nanoelectromagnetics applications," in *IEEE International Symposium on Electromagnetic Compatibility (EMC)*, Denver, Colorado (IEEE, 2013), pp. 376–379.
4. Y. Guo, T. Zhang, W.-Y. Yin, and X.-H. Wang, "Improved hybrid FDTD method for studying tunable graphene frequency-selective surfaces (GFSS) for THz-wave applications," IEEE Trans. Terahertz Sci. Technol. **5**, 358–367 (2015).
5. D.-W. Wang, W.-S. Zhao, X.-Q. Gu, W. Chen, and W.-Y. Yin, "Wideband modeling of graphene-based structures at different temperatures using hybrid FDTD method," IEEE Trans. Nanotechnol. **14**, 250–258 (2015).
6. G. D. Bouzianas, N. V. Kantartzis, T. V. Yioultsis, and T. D. Tsiboukis, "Consistent study of graphene structures through the direct incorporation of surface conductivity," IEEE Trans. Magn. **50**, 161–164 (2014).
7. X.-H. Wang, W.-Y. Yin, and Z. Chen, "Matrix exponential FDTD modeling of magnetized graphene sheet," IEEE Antennas Wireless Propag. Lett. **12**, 1129–1132 (2013).
8. V. Nayyeri, M. Soleimani, and O. M. Ramahi, "Modeling graphene in the finite-difference time-domain method using a surface boundary condition," IEEE Trans. Antennas Propag. **61**, 4176–4182 (2013).
9. R. de Oliveira, N. R. Rodrigues, and V. Dmitriev, "FDTD formulation for graphene modeling based on piecewise linear recursive convolution and thin material sheets techniques," IEEE Antennas Wireless Propag. Lett. **14**, 767–770 (2015).
10. A. Mock, "Padé approximant spectral fit for FDTD simulation of graphene in the near infrared," Opt. Mater. Express **2**, 771–781 (2012).
11. H. Lin, M. F. Pantoja, L. D. Angulo, J. Alvarez, R. G. Martin, and S. G. Garcia, "FDTD modeling of graphene devices using complex conjugate dispersion material model," IEEE Microwave Wireless Compon. Lett. **22**, 612–614 (2012).
12. A. Deinega and S. John, "Effective optical response of silicon to sunlight in the finite-difference time-domain method," Opt. Lett. **37**, 112–114 (2012).
13. A. Geim and I. Grigorieva, "Van der Waals heterostructures," Nature **499**, 419–425 (2013).
14. Q. H. Wang, K. Kalantar-Zadeh, A. Kis, J. N. Coleman, and M. S. Strano, "Electronics and optoelectronics of two-dimensional transition metal dichalcogenides," Nat. Nanotechnol. **7**, 699–712 (2012).
15. J. Cheng, W. L. Wang, H. Mosallaei, and E. Kaxiras, "Surface plasmon engineering in graphene functionalized with organic molecules: a multiscale theoretical investigation," Nano Lett. **14**, 50–56 (2014).
16. G. W. Hanson, "Dyadic green's functions for an anisotropic, non-local model of biased graphene," IEEE Trans. Antennas Propag. **56**, 747–757 (2008).
17. A. A. Oliner and A. Hessel, "Guided waves on sinusoidally-modulated reactance surfaces," IRE Trans. Antennas Propag. **7**, 201–208 (1959).
18. M. Esquius-Morote, J. S. Gomez-Diaz, and J. Perruisseau-Carrier, "Sinusoidally modulated graphene leaky-wave antenna for electronic beamscanning at THz," IEEE Trans. Terahertz Sci. Technol. **4**, 116–122 (2014).
19. J. Cheng, S. Jafar-Zanjani, and H. Mosallaei, "Real-time two-dimensional beam steering with gate-tunable materials: a theory design investigation," (2016). Manuscript submitted for publication to Scientific Reports.
20. P. Burghignoli, F. Frezza, A. Galli, and G. Schettini, "Synthesis of broad-beam patterns through leaky-wave antennas with rectilinear geometry," IEEE Antennas Wireless Propag. Lett. **2**, 136–139 (2003).
21. J. L. Gómez-Tornero, A. R. Weily, and Y. J. Guo, "Rectilinear leaky-wave antennas with broad beam patterns using hybrid printed-circuit waveguides," IEEE Trans. Antennas Propag. **59**, 3999–4007 (2011).
22. A. J. Martinez-Ros, J. L. Gomez-Tornero, and G. Goussetis, "Holographic pattern synthesis with modulated substrate integrated waveguide line-source leaky-wave antennas," IEEE Trans. Antennas Propag. **61**, 3466–3474 (2013).
23. B. Tierney and A. Grbic, "Arbitrary beam shaping using 1-d impedance surfaces supporting leaky waves," IEEE Trans. Antennas Propag. **63**, 2439–2448 (2015).
24. B. H. Fong, J. S. Colburn, J. J. Ottusch, J. L. Visher, and D. F. Sievenpiper, "Scalar and tensor holographic artificial impedance surfaces," IEEE Trans. Antennas Propag. **58**, 3212–3221 (2010).
25. J. Colburn, D. Sievenpiper, B. Fong, J. Ottusch, J. Visher, and P. Herz, "Advances in artificial impedance surface conformal antennas," in *IEEE Antennas and Propagation Society International Symposium* (IEEE, 2007), pp. 3820–3823.
26. Y. Zhang, J. Ouyang, K.-Z. Zhang, Y. Long, L.-J. Zhou, and F. Yang, "Conformal antennas based on holographic artificial impedance surfaces," in *IEEE Antennas and Propagation Society International Symposium (APSURSI)*, (IEEE, 2014), pp. 1552–1553.
27. M. Farmahini-Farahani and H. Mosallaei, "Functional-graded index metasurfaces for infrared radiation and guiding," IEEE Trans. Nanotechnol. **14**, 75–81 (2015).